Journal of Materials Chemistry C

ROYAL SOCIETY OF CHEMISTRY

PAPER

Supramolecular $Fe^{II}_4L_4$ cage for fast ammonia sensing†

Cite this: DOI: 10.1039/d2tc01655a

Weiyang Li,[a] Li Sun,[a] Cuilian Liu,[a] Aurelian Rotaru,[b] Koen Robeyns,[a] Michael Singleton[a] and Yann Garcia*[a]

Received 21st April 2022,
Accepted 14th May 2022

DOI: 10.1039/d2tc01655a

rsc.li/materials-c

The design and construction of colorimetric ammonia (NH_3) sensors with high selectivity, great stability and short response times at room temperature are highly needed for human health and food safety. We report herein a chiral supramolecular $Fe^{II}_4L_4$ metal-organic cage (MOC-1) able to detect $NH_{3(g)}$ at room temperature in less than 10 s, which we used to monitor food safety at 4 °C on fresh bacon bits. The detection is accompanied by a dramatic colour change from light brown to purple. In addition, MOC-1 exhibits superior selectivity among $NH_{3(g)}$ and twelve analytes including common solvents and amines. The reproducibility was studied by five continuous cyclic tests. Simple and low-cost smartphone-based and chemometrics analytical methods were used to study the sensing performance. The thermal stability is more than 200 °C. The sensing mechanism is associated with a high-spin to low-spin transition of the Fe^{II} ions, as expected for a ligand field strength that meets spin crossover conditions. These results show the high potential of MOC-1 as a convenient and inexpensive NH_3 gas sensor at room temperature, which could be used in the field of food safety assessment.

Introduction

Ammonia (NH_3) is widely used in agriculture, industry, medicine and so on.[1] However, even low concentrations of $NH_{3(g)}$ can impair the human immune system and cause serious medical issues.[2] 35 ppm for 10 mins was set by the U.S. Occupational Safety and Health Administration as the limit for exposure to $NH_{3(g)}$ in an indoor environment.[3] In addition, $NH_{3(g)}$ as an important component of total volatile basic nitrogen can be a potential indicator of the decomposition for high-protein foods, and therefore can be used as a tracker for food safety.[4] Hence, research on high-performance $NH_{3(g)}$ sensor materials and easy to operate, timely, and low-cost analytical methods is highly needed nowadays for human health.

Metal oxide-based sensors and conducting polymer-based sensors have been extensively studied due to their low cost, fabrication simplicity and good machinability.[5,6] Nevertheless, obvious shortcomings in selectivity, operation temperature and resistance measurements make them unsuitable for specific applications like food spoilage assessment or monitoring the surrounding environment.[7,8] Recently, metal–organic framework (MOF) materials were also applied as $NH_{3(g)}$ sensors. For instance, Dinca *et al.* reported MOFs with sensing ability to NH_3 at 100 °C based on the change of their associated luminescence, but no obvious $NH_{3(g)}$ sensing selectivity at room temperature (r.t.) was observed.[9,10] Zhang *et al.* reported a mixed-valence $Co^{II/III}$ MOF exhibiting high stability and reversibility. This system is however inaccurate due to the double colorimetric detection of $NH_{3(g)}$ and $H_2O_{(g)}$ molecules at r.t.[11]

Recently, Fe^{II} based coordination complexes have emerged as promising molecular sensing materials, because the coordination environment of the metal centre is sensitive to subtle changes triggered by guest molecule intercalation.[12] Meanwhile, optical outputs are altered by the spin state transition.[13] Our group reported two mononuclear high-spin (HS) complexes, $[Fe^{II}(trz\text{-}tet)_2(H_2O)_4]\cdot 2H_2O$ (trz-tetH = 5-(4*H*-1,2,4-triazol-yl)-2*H*-tetrazole) and $[Fe^{II}(H_2btm)_2(H_2O)_2]Cl_2$ (H_2btm = di(1*H*-tetrazol-5-yl)methane), respectively, as colorimetric sensors for various volatile organic compounds and hazardous gases under ambient conditions, but with slow response to $NH_{3(g)}$.[14–17] In addition, some Fe based spin crossover MOFs and hybrid materials were also reported for gas sensing (H_2O[18] and iodobenzene[19]) and food packaging applications.[20]

Herein, to improve the response time and stability of such molecular sensors, we introduce triazine-based ligands (*L* = (1*E*,1′*E*,1″*E*)-*N*,*N*′,N″-((1,3,5-triazine-2,4,6-triyl)tris(benzene-4,1-

[a] Institute of Condensed Matter and Nanosciences, Molecules, Solids, Reactivity (IMCN/MOST), Université Catholique de Louvain, Place Louis Pasteur 1, 1348 Louvain-la-Neuve, Belgium
[b] Department of Electrical Engineering and Computer Science and MANSiD Research Center, "Stefan cel Mare" University, University Street, 13, Suceava 720229, Romania

† Electronic supplementary information (ESI) available. CCDC 2157667. For ESI and crystallographic data in CIF or other electronic format see DOI: https://doi.org/10.1039/d2tc01655a

diyl))tris(1-(1-methyl-1*H*-imidazol-2-yl)methanimine)) to coordinate with Fe(II) ions to form a new polynuclear $Fe^{II}_4L_4$ metal-organic cage (**MOC-1**) with an Fe–N_6 coordination environment for $NH_{3(g)}$ sensing based on the following aspects: (i) introducing triazine-based ligands with multiple nitrogen sites as an electron acceptor into **MOC-1** was thought to increase the $NH_{3(g)}$ uptake ability and selectivity;[21] (ii) the presence of the porous structure can improve the $NH_{3(g)}$ diffusion rate and enhance the sensitivity of the sensor; (iii) using a rapid precipitation method to prepare microcrystalline materials with increased specific surface area and active sites to enhance the sensitivity for $NH_{3(g)}$; (iv) the FeN_6 coordination sphere in each Fe^{II} metal centre may not be easily replaced by guest NH_3 molecules, which gives robustness compared to reported Fe^{II} based sensors with H_2O molecules participating in coordination. As expected, **MOC-1** was found to exhibit superior selectivity among common solvents and amines and short response times (10 s for $NH_{3(g)}$ vapor) with noticeable colour switching at r.t. In addition, the thermal stability of **MOC-1** is more than 200 °C. ^{57}Fe Mössbauer spectroscopy was used to study the sensing mechanism, which revealed a spin state transition of the Fe^{II} metal centres after adsorption of $NH_{3(g)}$ molecules. Moreover, we employed simple and convenient smartphone-based and chemometrics analytical methods including hierarchical clustering analysis (HCA) and principal component analysis (PCA), to study the sensing performance, replacing traditional detection methods such as gas chromatography and spectrophotometry that require extensive instrumentation and complicated analytical methods, making **MOC-1** accessible for *in-field* applications. A proof of concept experiment was carried out to monitor pork spoilage at 4 °C (fridge conditions) successfully.

Results and discussion

MOC-1 was prepared by subcomponent self-assembly reaction of $Fe(BF_4)_2{\cdot}6H_2O$, 2,4,6-tris-(4-aminophenyl)triazine (TATP) and 1-methyl-2-imidazolecarboxaldehyde in 4 : 4 : 12 stoichiometry in acetonitrile. After diffusion of diethyl ether into the reaction solution for several days, red block like crystals were obtained (ESI†). Single crystal X-ray diffraction at 100 K revealed that **MOC-1** crystallized in the monoclinic *Ia* space group, and the unit cell volume was 79448(9) Å^3. As shown in Fig. 1a, each Fe^{II} centre is coordinated with six nitrogen atoms from three imidazole-imine type ligands, forming an octahedral FeN_6 coordination geometry. The tetrahedron is constructed by four C_3-symmetric ligands located on its faces and four Fe centres occupying its vertices. Crystallographic parameters are summarized in Table S1 (ESI†). Interestingly, one BF_4^- anion is trapped in the cavity of the cage and the other seven BF_4^- anions are located around the periphery. Terminal F atoms act as hydrogen bond acceptors for the ligand C–H donors, resulting in the formation of an extensive hydrogen bonding network throughout the crystal lattice (Fig. 1b). A large amount of diethyl ether was poured into the reaction solution to obtain

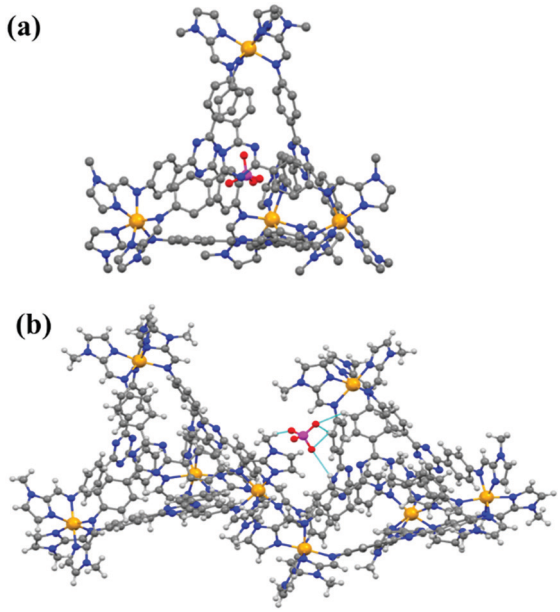

Fig. 1 (a) Crystal structure of **MOC-1** at 100 K. One BF_4^- counter anion is in the cavity of the cage. The given tetrahedron is either of ΔΔΔΔ or ΛΛΛΛ chirality at the Fe(II) centres, with adjacent tetrahedra being of opposite chirality; (b) the hydrogen bond scheme in **MOC-1**. C: dark grey; N: blue; and Fe: yellow; B: magenta; F: red; H: white.

microcrystalline **MOC-1** for sensing experiments. Powder X-ray diffraction (PXRD) exhibited an amorphous pattern (Fig. S1, ESI†), in agreement with particle clustering as detected in scanning electronic microscopy (Fig. S2, ESI†). High resolution mass spectrometry (HRMS) revealed molecular ion peaks at *m*/*z* 343.23 corresponding to $[Fe_4L_4]^{8+}$, further proving the discrete polynuclear nature of **MOC-1**. The molecular formula of **MOC-1** was confirmed by elemental analysis with $Fe^{II}_4L_4(BF_4)_8{\cdot}9H_2O$. Fe, N, O, B, F and C signals were observed in the XPS spectrum, and no impurity was evidenced (Fig. S3, ESI†). The Fe/N = 0.10 is in close agreement with coordination of Fe^{II} through a triazine-based ligand motif (calculated Fe_4/N_{48} = 0.08). In the Fe 2p core spectrum, two distinct peaks located at 723.3 eV and 709.7 eV (Fig. S4, ESI†) correspond to Fe $2p_{1/2}$ and Fe $2p_{3/2}$ of **MOC-1**, respectively.[22] In addition, a broad shoulder at 714.4 eV is ascribed to the satellite peak for Fe $2p_{3/2}$ because of the existence of HS Fe^{II} in **MOC-1**, which is well expected for such ligand systems.[22] The FT-IR spectrum of **MOC-1** (Fig. S5, ESI†) showed typical absorptions for the stretching of the imidazole-imine (C=N) groups at 1584 cm^{-1} and the peaks at about 1056 and 1014 cm^{-1} proved the existence of BF_4^-.[14,23]

The thermogravimetric analysis (TGA) of **MOC-1** showed a continuous mass loss of *ca.* 4.2% from r.t. to 200 °C (Fig. S6, ESI†), which is assigned to the release of 9 H_2O molecules, matching well the CHN result (4.5%). Above 200 °C, a platform was observed until *ca.* 300 °C indicating a high thermal stability. The stability was also tracked by variable-temperature Raman spectroscopy (Fig. 2) by focusing on the C=N vibration located at 1590 cm^{-1}.[24] The peak was observed from 30 °C up to 200 °C, but disappeared at 250 °C, in good

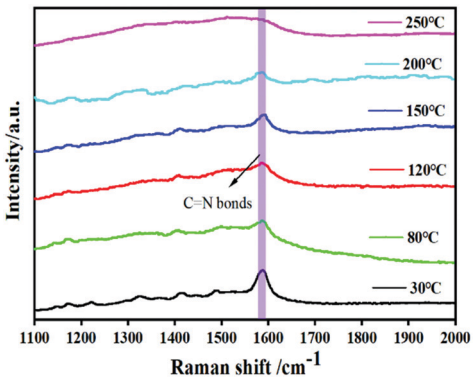

Fig. 2 Variable-temperature Raman spectra of MOC-1.

agreement with TGA measurements, which were run in scanning mode.

Standard chemometric methods were performed to compare the colour dissimilarity of **MOC-1** to 13 saturated analyte vapours at r.t. HCA, an unsupervised method based on the grouping of the analyte vectors according to their spatial distances in their full original vector space, was employed using the minimum variance (Ward's) method for different analytes.[25] In this work, 6-dimensional colour vectors including RGB (red, green, and blue) and HSB1 (hue, saturation, and brightness) were studied. As shown in Fig. 3a (Table S2 and Fig. S7a, ESI†), two colour clusters were identified, but one group was occupied only by $NH_{3(g)}$, indicating the superior selectivity of the sensor among common solvents and amines alone. Another chemometric method, PCA,[25] was also used to group the same multidimensional data set. The scree plots (Fig. S8a and Table S3, ESI†) show that two dimensions are required to capture 98% of the total variance. The PCA score plots based on the first two principal components (PC1 and PC2) show similar results to those from HCA: two fully separable clustering was observed, which confirmed the selectivity of our sensor towards $NH_{3(g)}$ (Fig. S8b, ESI†). **MOC-1** showed a fast response to $NH_{3(g)}$ since the powder turned from light brown to purple in 10 s and kept its colour until 240 s (Fig. 3b). The diffuse reflectance spectrum of **MOC-1** exhibited a relatively weak broad band at 530 nm, which is assigned to metal-to-ligand (MLCT) transition for Fe(II) centres coordinated to imidazole-imine based ligands.[26] A clear shift of the optical adsorption band can be observed in **MOC-1**@NH_3. The high-intensity broad band around λ = 565 nm is attributed to the $^1A_1 \rightarrow {}^1T_1$ *d–d* transition of the low-spin state in the Fe(II) compound,[14,17] in agreement with the analysis of ^{57}Fe Mössbauer spectroscopy (discussed later). Diffuse reflectance spectra of the other analytes except $NH_{3(g)}$ are shown in Fig. S7b, (ESI†) where no significant optical absorption peak shift is observed. The improved response speed compared with reported Fe(II) complex sensors may be attributed to the cavity structure and the large specific surface area, which presumably increases the diffusion rate of $NH_{3(g)}$. Because of the coexistence of $NH_{3(g)}$ and $H_2O_{(g)}$ in any ammonia solution, **MOC-1** was exposed to different relative humidity (RH) alone and NH_3 vapor in different RH to assess its

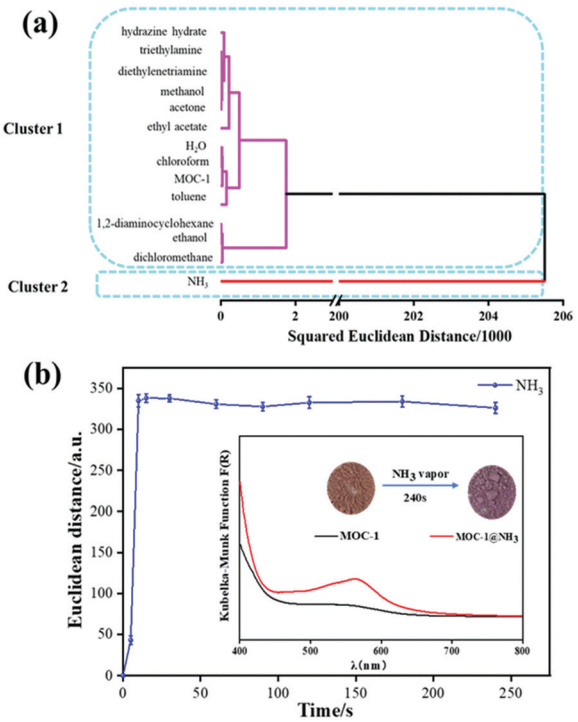

Fig. 3 (a) HCA dendrogram for **MOC-1**, $NH_{3(g)}$ and 12 analytes at full vapor pressure at r.t.; (b) response time of **MOC-1** to $NH_{3(g)}$ under vapor diffusion at r.t. Inset: Diffuse reflectance spectroscopy and digital photographs of **MOC-1** and **MOC-1**@NH_3 (exposure for 240 s). The Euclidean distances are defined by the colour vectors in the full 6-dimensional space including RGB (red, green, and blue) and HSB1 (hue, saturation, and brightness).

antihumidity interference ability during the sensing process (Fig. S9 and Table S4, ESI†). Clearly, under RH from 35 to 85% alone, negligible change of the Euclidean distances was observed, demonstrating that water in ammonia solution has little effect on the sensing process. When **MOC-1** was exposed NH_3 vapor in 65% RH, the Euclidean distances were similar to the value in 25% RH (normal condition), which indicates that **MOC-1** has good resistance to moisture. In addition, **MOC-1** was exposed to a mixture of 12 analyte vapours and $NH_{3(g)}$ to observe whether interfering analyte vapours would influence ammonia sensing at r.t. (Fig. S10 and Table S5, ESI†). The values of the Euclidean distance are very similar in the mixed vapor atmosphere to $NH_{3(g)}$ alone, in contrast to other individual analyte vapours, indicating that **MOC-1** displays good selectivity for ammonia in a mixed atmosphere.

Our sensor showed a good cyclability after 5 adsorption and desorption processes of $NH_{3(g)}$ (Table S6 and Fig. 4a, Fig. S11, ESI†). The regeneration process was also monitored by FT-IR spectroscopy (Fig. 4b). The appearance of the band at 1610 cm^{-1} in **MOC-1**@NH_3 is characteristic of N–H bending, indicative of the presence of $NH_{3(g)}$.[27] However, after the desorption process (by heating in vacuum at 70 °C overnight), the band disappeared in regenerated **MOC-1** and the shape of the spectrum was consistent with **MOC-1**. No new phase was detected by PXRD for the regenerated **MOC-1** (Fig. S12, ESI†).

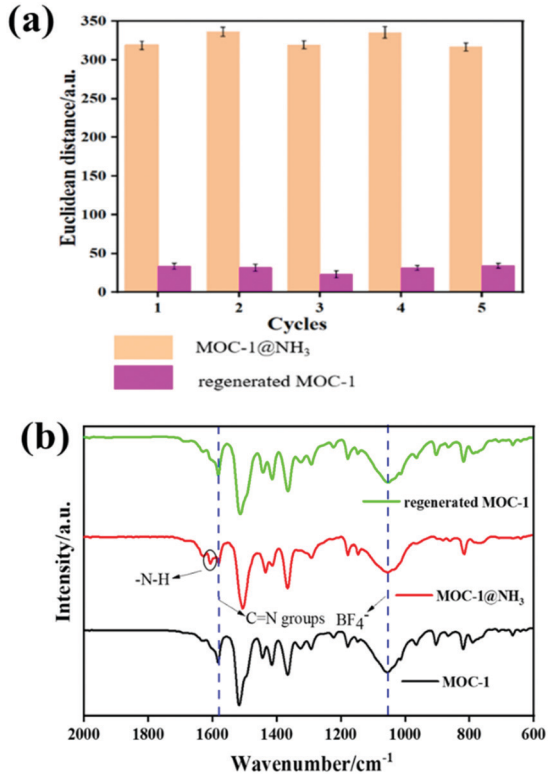

Fig. 4 (a) Recyclability test for the **MOC-1** sensor; (b) FT-IR spectra for **MOC-1**, **MOC-1**@NH_3 and regenerated **MOC-1**.

In addition, ^{57}Fe Mössbauer spectroscopy for the regenerated **MOC-1** also exhibited three quadrupole doublets for LS, HS-1 and HS-2 and the LS/HS Fe^{II} ratio is 33 : 67%, which is almost the same as that of **MOC-1** (29 : 71%) (Fig. S13, ESI†). Thus, the structure and the spin states of Fe(II) ions during the regeneration process are maintained, revealing superior reversibility of the sensor.

We estimated the limits of detection (LODs) of $NH_{3(g)}$ through fitting of the response curve (which gives a good linearity, R^2 = 0.99) and extrapolation of the curve to a concentration where the sensor response is 3 times that of the noise level (*i.e.*, S/N = 3)[28] (Fig. S14 and Table S7, ESI†). The noise was defined as the standard deviation among the control. LODs were calculated to be 2.8 ppm, which is well below the suggested exposure limits for human body in an indoor environment. For comparison, we summarized the sensing performance and detection technology of the MOC-1 sensor and other traditional NH_3 sensors such as the metal oxide conducting polymer, and MOFs, as listed in Table S8 (ESI†). This result indicated that MOC-1 exhibited high detection sensitivity towards $NH_{3(g)}$ at r.t. and the smartphone-based analytical method was simple, convenient and time-saving without complicated detection technologies and sophisticated instrumentation such as fluorescence spectroscopy[29] and resistance measurement.[4]

^{57}Fe Mössbauer spectroscopy measurements on **MOC-1** and **MOC-1**@NH_3 were run to assess the sensing mechanism and probe the spin and oxidation states of this material (Table 1).

Table 1 ^{57}Fe Mössbauer parameters for **MOC-1** and **MOC-1**@NH_3

			Mössbauer parameters		
Sample	Spin state Fe(II)	A/A_{tot} (%)	δ (mm s^{-1})	ΔE_Q (mm s^{-1})	$\Gamma/2$
MOC-1	LS (blue)	29	0.20(3)	0.70(1)	0.25(1)
	HS-1 (red)	44	0.99(1)	1.39(1)	0.20(1)
	HS-2 (magenta)	27	1.10(4)	2.60(1)	0.30(1)
MOC-1@NH_3	LS (blue)	60	0.27(1)	0.66(1)	0.28(1)
	HS-1 (red)	20	0.96(1)	1.45(2)	0.21(1)
	HS-2 (magenta)	20	1.29(4)	2.19(1)	0.28(1)

The spectrum of **MOC-1** reveals three quadrupole doublets (Fig. 5a). The first one [isomer shift δ = 0.20(3) mm s^{-1}; quadrupole splitting ΔE_Q = 0.70(1) mm s^{-1}] is characteristic of low-spin (LS) Fe^{II} ions, with an area fraction (A) of 29%. The two other doublets HS-1 [δ = 0.99(1) mm s^{-1}; ΔE_Q = 1.39(1) mm s^{-1}; A = 44%] and HS-2 [δ = 1.10(4) mm s^{-1}; ΔE_Q = 2.60(1) mm s^{-1}; A = 27%] correspond to high-spin (HS) Fe^{II} ions. The LS/HS Fe^{II} ratio is 29 : 71%. Similar parameters can be found in other Fe^{II} complexes with N_6 donor sets.[30–32] After sensing NH_3 molecules, the Mössbauer spectrum of **MOC-1**@NH_3 also exhibits three quadrupole doublets: [δ = 0.27(1) mm s^{-1}; ΔE_Q = 0.66(1) mm s^{-1}; A = 60%]; [δ = 0.96(1) mm s^{-1}; ΔE_Q = 1.45(2) mm s^{-1}; A = 20%]; [δ = 1.29(4) mm s^{-1}; ΔE_Q = 2.19(1) mm s^{-1}; A = 20%], corresponding to LS, HS-1 and HS-2 Fe(II) ions,

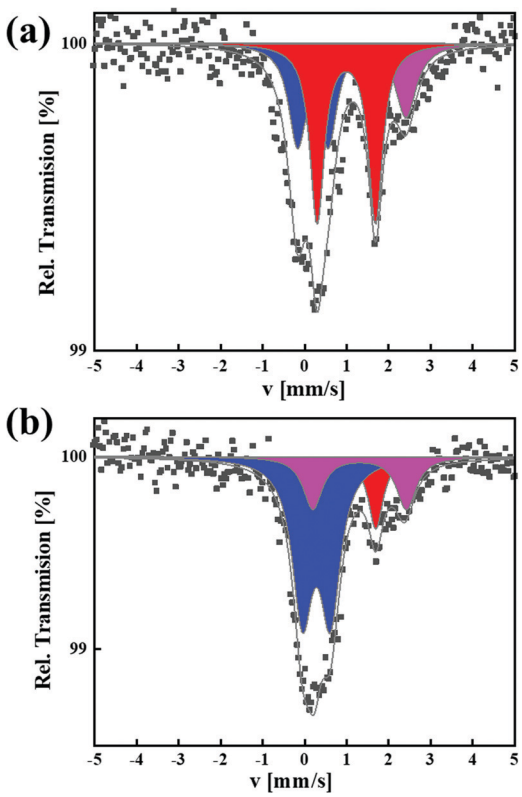

Fig. 5 ^{57}Fe Mössbauer spectra of **MOC-1** (a) and **MOC-1**@NH_3 (b) recorded at 298 K. The red, magenta and blue quadrupole doublets correspond to HS-1, HS-2 and LS Fe(II) ions, respectively.

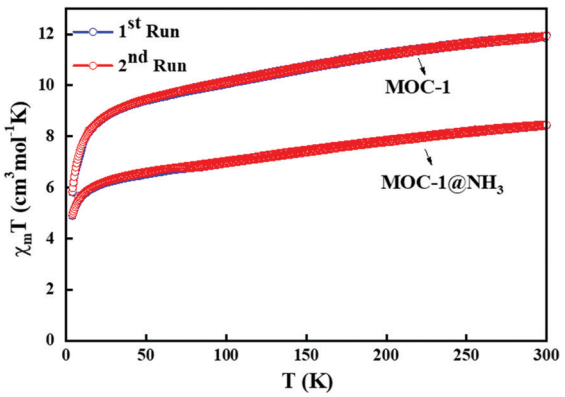

Fig. 6 Temperature-dependent $\chi_m T$ *vs.* *T* plots for **MOC-1** and **MOC-1**@NH_3.

respectively (Fig. 5b). The LS/HS ratio changed significantly to 60 : 40%. No traces of oxidation or oxides were detected up to 10 mm s^{-1} in our spectra. Therefore, the sensing mechanism of **MOC-1** was ascribed to the transition of the spin state of Fe^{II} ions after intrusion of $NH_{3(g)}$ molecules. On cooling, **MOC-1** exhibits gradual spin crossover and thermochromic properties (Fig. 6 and Fig. S15, ESI†), which means that the ligand field strength can be modified by external stimuli on this system. The $\chi_m T$ undergoes a decrease from 11.92 cm^3 mol^{-1} K for **MOC-1** to 8.43 cm^3 mol^{-1} K for **MOC-1**@NH_3 at 298 K, indicating a loss of HS state, which is consistent with the Mössbauer spectrum data. The imine linker and triazine ring in the ligands can serve as active sites for NH_3 adsorption, resulting in a change in the electronic structure of the sensor.[33,34] In addition, after solvent exchange with atmosphere, as observed on **MOC-1** powder, free water molecules may be replaced by NH_3 molecules and affect the coordination environment around the iron, further affecting the spin state. Thus, we infer that the cause of the spin state transition is due either to the formation of hydrogen bonds between NH_3 molecules and *N*-rich ligands or the substitution of water molecules by NH_3 molecules (Fig. S16, ESI†). PXRD of **MOC-1**@NH_3 was not modified (Fig. S17, ESI†) confirming the structural integrity. We have tried to prepare single crystals containing NH_3 molecules using a single crystal to single crystal transformation, but it was not successful due to the instability of the crystals at room temperature.

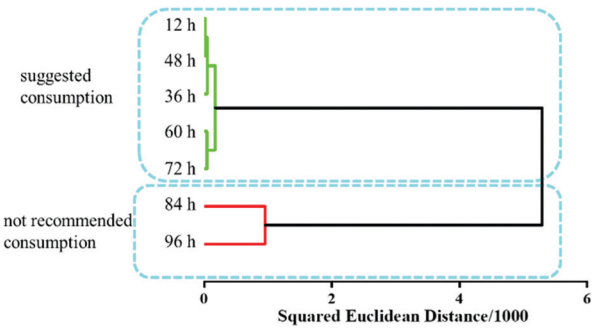

Fig. 7 HCA dendrogram for the pork spoilage experiment at different time intervals.

Due to the remarkable sensitivity of **MOC-1**, we thought to use it as an indicator to monitor the spoilage of pork at 4 °C, a typical storage temperature for fresh meat on the shelf. The detailed methodology is provided in the ESI.† At specific time intervals, photographs of the sensor were taken, and these data were treated by HCA (Table S9, ESI†). As shown in the dendrogram (Fig. 7), the data were categorized into two clusters (12–72 h and 84–96 h), indicating that **MOC-1** presents two different colours on sensing. The results suggest that the meat would be best eaten within 72 h, and starts to spoil at 84 h and is best discarded. A commercial ammonia sensor (AR8500) was used to detect the concentration at each time interval. Considering that there is no clear reference standard for the $NH_{3(g)}$ concentration at each stage of spoilage, the time of rapid concentration increase can be considered as the beginning of the decay process.[35] As shown in Fig. S18, (ESI†) before 72 h, no ammonia release was detected by the sensor, indicating that the food was fresh. However, at 84 h and 96 h the concentration of $NH_{3(g)}$ appeared to increase rapidly from 7.8 ppm to 16.4 ppm, indicating that the pork was starting to spoil and was not recommended for consumption, which is consistent with the HCA results. Thus, **MOC-1** shows great potential in meat safety assessment, be it for food transport or in food storage in household fridges, after opening of the meat packaging.

Conclusions

In summary, a chiral $Fe^{II}_4L_4$ metal organic cage (**MOC-1**) with *N*-rich ligands was successfully prepared for $NH_{3(g)}$ sensing under ambient conditions. The fabricated **MOC-1** sensor exhibits superior sensitivity and excellent selectivity to earlier literature reports. It also possesses high stability and reproducibility over five cyclic experiments. The discolouration mechanism is ascribed to the change of the spin state ratio of Fe^{II} ions after adsorption of NH_3 molecules, which possibly are connected to *N*-rich ligands *via* hydrogen bonds. Furthermore, we combined colorimetric sensor detection with a smartphone-based analytical method to develop **MOC-1** as an indicator for monitoring pork meat spoilage at 4 °C, which showed great potential in the field of meat storage and transportation.

Conflicts of interest

There are no conflicts to declare.

Acknowledgements

This work was supported by the Fonds De La Recherche Scientifique—FNRS (CDR 33694457, PDR T.0095.21) the Ministère de l'Education et de la Recherche de Roumanie and WBI (PN-III-CEI-BIM-PBE-2020-0042/8BM/2021). W. L., C. L. and L. S. were supported by fellowships from the China Scholarship Council (201908310083, 201704910812 and 201804910584).

References

1 B. Timmer, W. Olthuis and A. V.-D. Berg, *Sens. Actuators, B*, 2005, **107**, 666–677.
2 X. Liu, N. Chen, B. Han, X. Xiao, G. Chen, I. Djerdj and Y. Wang, *Nanoscale*, 2015, **7**, 14872–14880.
3 S. Bai, Y. Zhao, J. Sun, Y. Tian, R. Luo, D. Li and A. Chen, *Chem. Commun.*, 2015, **51**, 7524–7527.
4 D. Zhang, S. Yu, X. Wang, J. Huang, W. Pan, J. Zhang, B. E. Meteku and J. Zeng, *J. Hazard. Mater.*, 2022, **423**, 127160.
5 G. H. Mhlongo, D. E. Motaung, F. R. Cummings, H. C. Swart and S. S. Ray, *Sci. Rep.*, 2019, **9**, 9881.
6 Y. Chen, W. Zhang and Q. Wu, *Sens. Actuators, B*, 2017, **242**, 1216–1226.
7 N. Van Hieu, N. Q. Dung, P. D. Tam, T. Trung and N. D. Chien, *Sens. Actuators, B*, 2009, **140**, 500–507.
8 M. Matsuguchi, A. Okamoto and Y. Sakai, *Sens. Actuators, B*, 2003, **94**, 46–52.
9 N. B. Shustova, A. F. Cozzolino, S. Reineke, M. Baldo and M. Dinca, *J. Am. Chem. Soc.*, 2013, **135**, 13326–13329.
10 M. G. Campbell, D. Sheberla, S. F. Liu, T. M. Swager and M. Dinca, *Angew. Chem., Int. Ed.*, 2015, **54**, 4349–4352.
11 J. Zhang, J. Ouyang, Y. Ye, Z. Li, Q. Lin, T. Chen, Z. Zhang and S. Xiang, *ACS Appl. Mater. Interfaces*, 2018, **10**, 27465–27471.
12 R. Ohtani and S. Hayami, *Chem. – Eur. J.*, 2017, **23**, 2236–2248.
13 D. Gentili, N. Demitri, B. Schäfer, F. Liscio, I. Bergenti, G. Ruani, M. Ruben and M. Cavallini, *J. Mater. Chem. C*, 2015, **3**, 7836–7844.
14 A. D. Naik, K. Robeyns, C. F. Meunier, A. F. Leonard, A. Rotaru, B. Tinant, Y. Filinchuk, B. L. Su and Y. Garcia, *Inorg. Chem.*, 2014, **53**, 1263–1265.
15 Y. Guo, S. Xue, M. M. Dîrtu and Y. Garcia, *J. Mater. Chem. C*, 2018, **6**, 3895–3900.
16 S. Xue, L. Wang, A. D. Naik, J. Oláh, K. Robeyns, A. Rotaru, Y. Guo and Y. Garcia, *Inorg. Chem. Front.*, 2021, **8**, 3532–3546.
17 L. Sun, A. Rotaru, K. Robeyns and Y. Garcia, *Ind. Eng. Chem.*, 2021, **60**, 8788–8798.
18 Z. G. Lada, K. S. Andrikopoulos, G. N. Mathioudakis, Z. Piperigkou, N. Karamanos, S. P. Perlepes and G. A. Voyiatzis, *Magnetochemistry*, 2022, **8**, 16.
19 A. Tissot, X. Kesse, S. Giannopoulou, I. Stenger, L. Binet, E. Rivière and C. Serre, *Chem. Commun.*, 2019, **55**, 194.
20 C. Bartual-Murgui, A. Akou, C. Thibault, G. Molnar, C. Vieu, L. Salmon and A. Bousseksou, *J. Mater. Chem. C*, 2015, **3**, 1277–1285.
21 L. Tao, F. Niu, D. Zhang, T. Wang and Q. Wang, *New J. Chem.*, 2014, **38**, 2774–2777.
22 A. R.-C. Li, R. Akiyoshi, A. Tsukiashi, S. Hayami, O. Mustonen, M. M. Bhadbhade, S. Bhattacharyya, C. E. Marjo, Y. Wang, L. F. Lindoy, J. R. Aldrich-Wright and F. Li, *Dalton Trans.*, 2018, **47**, 2543–2548.
23 H. X. Zhang, X. Yan, Y. X. Chen, S. H. Zhang, T. Li, W. K. Han, L. Y. Bao, R. Shen and Z. G. Gu, *Chem. Commun.*, 2019, **55**, 1120–1123.
24 W. Dai, F. Shao, J. Szczerbinski, R. McCaffrey, R. Zenobi, Y. Jin, A. D. Schluter and W. Zhang, *Angew. Chem., Int. Ed.*, 2016, **55**, 213–217.
25 K. Diehl and E. Anslyn, *Chem. Soc. Rev.*, 2013, **42**, 8596–8611.
26 L. Li, N. Saigo, Y. Zhang, D. J. Fanna, N. D. Shepherd, J. K. Clegg, R. Zheng, S. Hayami, L. F. Lindoy, J. R. Aldrich-Wright, C. Li, J. K. Reynolds, D. G. Harman and F. Li, *J. Mater. Chem. C*, 2015, **3**, 7878–7882.
27 J. B. DeCoste, M. S. Denny, Jr., G. W. Peterson, J. J. Mahle and S. M. Cohen, *Chem. Sci.*, 2016, **7**, 2711–2716.
28 Z. Li and K. S. Suslick, *ACS Appl. Mater. Interfaces*, 2018, **10**, 15820–15828.
29 X. Chen, Y. Yu, C. Yang, J. Yin, X. Song, J. Li and H. Fei, *ACS Appl. Mater. Interfaces*, 2021, **13**, 52765–52774.
30 M. Nihei, M. Ui, M. Yokota, L. Han, A. Maeda, H. Kishida, H. Okamoto and H. Oshio, *Angew. Chem., Int. Ed.*, 2005, **117**, 6642–6645.
31 B. Schneider, S. Demeshko, S. Neudeck, S. Dechert and F. Meyer, *Inorg. Chem.*, 2013, **52**, 13230–13237.
32 S. Xue, Y. Guo, A. Rotaru, H. Muller-Bunz, G. G. Morgan, E. Trzop, E. Collet, J. Olah and Y. Garcia, *Inorg. Chem.*, 2018, **57**, 9880–9891.
33 F. Niu, Z.-W. Shao, L.-M. Tao and Y. Ding, *Sens. Actuators, B*, 2020, **321**, 128513.
34 F. Niu, Z.-W. Shao, J.-L. Zhu, L.-M. Tao and Y. Ding, *J. Mater. Chem. C*, 2021, **9**, 8562–8569.
35 C. Cai, J. Mo, Y. Lu, N. Zhang, Z. Wu, S. Wang and S. Nie, *Nano Energy*, 2021, **83**, 105833.